https://doi.org/10.1016/j.ensm.2023.102805

Discovering the Pore-filling of Potassium Ions in Hard Carbon Anodes: Revisit the Low-Voltage Region

ABSTRACT Hard carbon anodes deliver attractive performance because of abundant active sites for hosting the charge. Among diverse charge storage mechanisms, pore-filling is of particular interest in emerging Na/K ion batteries owing to the induced high capacity at a low voltage. Despite the widely accepted Na ion pore-filling, whether K ion could fill in the nanopores remains vague. We explore the K storage behavior associated with the different voltage regions taking pistachio shell-derived hard carbon as a model. Besides the reported adsorption and intercalation mechanisms at relatively high potentials, cryo-transmission electron microscopy and electron paramagnetic resonance indicates the presence of quasi-metallic potassium nanoclusters once discharged continuously at 5 mV *vs.* K^+/K, unambiguously demonstrating the K ion pore-filling in hard carbon anodes. We also discuss the strategies to promote such behavior, and show that chemical etching-induced open pores could boost the kinetics but not benefit the capacity. Developing high-capacity hard carbon anodes relies on the rational design of closed pores.

KEYWORDS Potassium ion battery; Hard carbon; Charge storage mechanism; Pore-filling behavior

1. Introduction

Lithium-ion batteries (LIBs), as the dominant energy storage devices for portable electronics and hybrid electric vehicles, have encountered some "bottleneck" issues on the soaring cost of raw materials and the shortage of Li resources[1]. K-ion batteries (KIBs), with characteristics of abundant K in the earth's crust (about 400 times of Li abundance)[2, 3], the close redox potential with Li and the capability of using Al as the current collector for anodes, are promising candidates for large-scale energy storage. Inherited from the Li-ion counterpart, carbon materials are among the most attractive anodes for KIBs. Compared to Na ions, it is a delight to find the K ions could be intercalated into graphitic carbon. However, the insertion of K^+ with a large radius (1.33 Å *vs.* 0.68 Å for Li^+) often causes severe volume expansion[4], i.e., about 61% for KC_8 formation compared to 10% for LiC_6. Such a large distortion damages the layered structure of graphite, leading to unsatisfactory cyclability and rate performance if not well protected[5].

Other carbon materials possess diverse active sites for hosting alkali metal ions. Along with the intercalation, other charge storage mechanisms are also widely explored to boost performance, in particular for the hard carbon anodes with rich composition and morphology[6]. For instance, surface adsorption on defects has been utilized to enhance the rate capability because of the fast kinetics[7, 8]. However, these sites normally uptake K ions at a relatively high potential[9], discouraging the construction of high-voltage KIBs when coupling with cathodes. This is clearly reflected in low-cost biomass-derived hard carbon materials[10, 11] whose large proportion of the capacity is gained generally at over 1 V (as summarized in **Table S1**). An in-depth understanding of the K ion uptake mechanism in the low-potential region and enhancing the low-voltage capacity are therefore the keys to achieving high-performance hard carbon anodes for KIBs.

The situation significantly differs from the Na ion storage in hard carbon, which shows an essential fraction of capacity at a low voltage plateau of ~0.1 V *vs.* Na^+/Na[12], making it the most attractive anode for practical application. The low-voltage capacity is associated with the Na ion filling in the nanopores, evidenced by the presence of a quasi-metallic sodium clusters signal in nuclear magnetic resonance (NMR) spectra[13]. Most recently, Yang's group[14] reported the possible K ion pore-filling by comparing the Na and K ion storage using electron paramagnetic resonance (EPR). There is still a lack of any direct evidence, despite an open call for deep investigation[15, 16], to confirm whether a pore-filling mechanism occurs in KIBs, bringing difficulty to rational microstructure design.

Herein, we synthesize porous and partially ordered HC from pistachio shucks biomass waste. It exhibits a charging capacity (K ion extraction) of around 220 mAh g^{-1} under 1.0 V, outperforming most reported biomass waste-derived carbon (**Table S1**). In addition to the K ion adsorption in the sloping region of the voltage profiles, an "intercalation-pore filling" hybrid behavior of K ions in hard carbon is detected in the low-potential region. The universality of such behavior is confirmed in lignin-derived HC. This clarified mechanism elucidates the current blurring understanding of K ion storage and offers new insights into designing advanced hard carbon anodes for KIBs.

2. Results and discussion

2.1 Synthesis and physical properties of hard carbon

As **Figure 1a** illustrated, the rinsed pistachio shucks were first ball-milled to fine powder, then sintered into uniform and dark ones. HCl treatment was applied after the calcination to remove impurities, as proved by X-ray diffraction (XRD) in **Figure S1**. X-ray photoelectron spectroscopy (XPS) pattern (**Figure S2**) further confirms the absence of impurity atoms other than oxygen, which is widely probed as surface functional groups and may contribute to K ion storage. Raman

results (**Figure S3a**) show a high intensity of D band at around 1341 cm^{-1} because of the poor crystallinity and partially ordered domain under moderate carbonization temperatures of 1100-1400 ºC, which agrees with the XRD broad peaks at ~22° and 43° (**Figure S3b**) representing (002) and (100) diffraction. The sample treated at 1300 ºC (denoted as HC-1300) delivers the highest capacity of 273 mAh g^{-1} with a retention of 96.7% (**Figure S3c-d**) and is selected for probing the charge storage mechanism.

The structural feature of HC-1300 is captured by cryo-electron transmission microscopy (cryo-TEM), which confirms the partially ordered structure exhibiting small graphitic domains and isolated graphene layers (**Figure 1b**). The small-angle X-ray scattering (SAXS) technique sensitive to both closed and open pores is employed for exploring the overall pore information. The data is fitted through the correlation between the characteristic length and the scattering power variation (**Figure 1c**)[17]. It confirms the presence of meso- and micro-pores in the sample (**Figure S4-5**), leading to a large surface area S_{SAXS} of 229.0 m^2 g^{-1}. The pore distribution is further investigated by the N_2 adsorption/desorption (**Figure 1d**). It shows a Brunauer-Emmett-Teller (BET) surface area of 1.7 m^2 g^{-1} and a pore volume of 0.004 cm^3 g^{-1}. The pore size concentrates at 1.4 nm (micropores), 9.3 nm (mesopores), and over 50 nm (macropores), with an average pore size of 9.4 nm. Since N_2 adsorption has limitations in detecting the ultra-micropores, CO_2 adsorption is adopted as the supplementary. The CO_2 adsorption test result gives a much higher surface area of 70.9 m^2 g^{-1} and a pore volume of 0.008 cm^3 g^{-1} (**Figure 1e**). It implies that apart from larger pores, a large content of micropores exist inside HC-1300, whose size is centered at 0.52-0.77 nm.

Note that the surface area obtained in N_2 and CO_2 adsorption/desorption is much smaller than that derived from SAXS. The reason lies in that the former two techniques mainly provide

information on open pores[18]. The results indicate that substantial amounts of closed pores are presented in HC-1300. By subtracting S_{BET} from S_{SAXS}, the surface area contributed by the closed pore is as high as 158.1 $m^2\ g^{-1}$. Furthermore, we examine the volume of closed pores through the true density measurement by the helium pycnometer since the He atom can reach nearly all pores in the samples (Details are in **Figure S5**). The volume of closed pores is calculated to be 0.043 $cm^3\ g^{-1}$ based on the true density of the sample (ρ_{true}=2.06 g cm^{-3}), which is over five times that of open pores obtained in CO_2 adsorption/desorption. The rich porosity (as summarized in **Table S2**) provides a platform for exploring whether potassium nanocluster could be stored through the pore-filling mechanism.

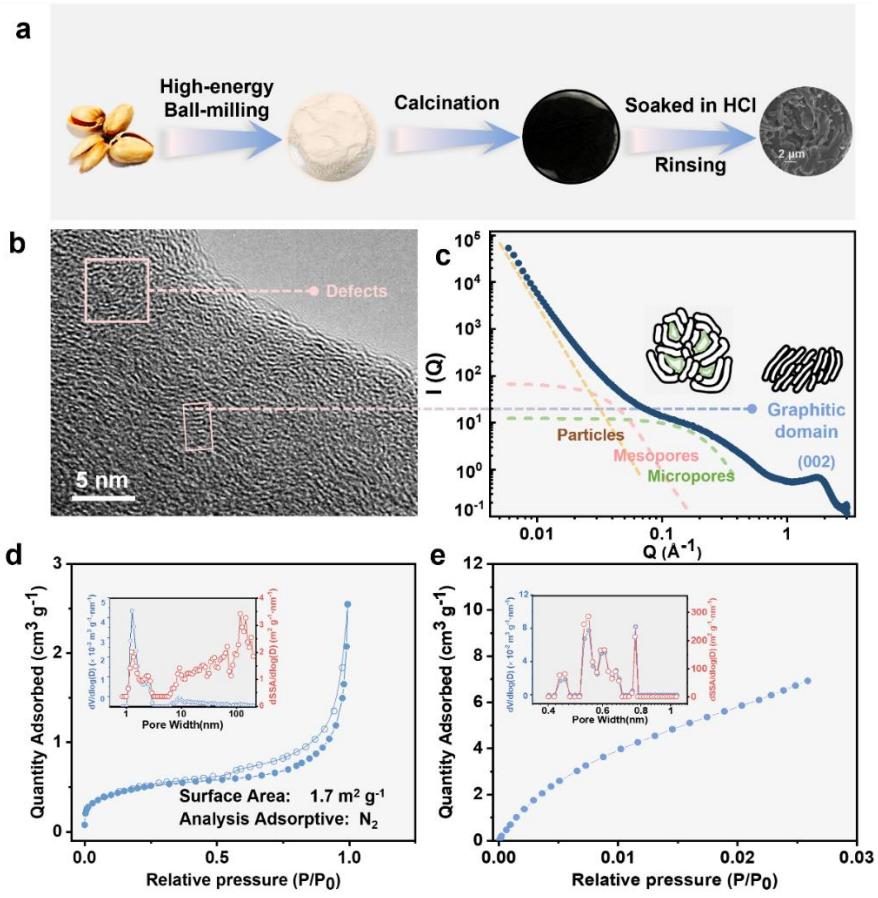

Figure 1. Synthesis and structural information of hard carbon. (a) Synthesis procedure of hard carbon; (b) HRTEM with marked defects (the left square), graphitic domain (rectangle in the

middle); (c) SAXS patterns presenting pores and graphitic layers; BET isotherms with porosity distribution derived from (d) N_2 and (e) CO_2 adsorption/desorption.

2.2 Electrochemical performance and kinetics

We first compare the K ion storage with the Na counterpart, as the latter could be readily stored through pore-filling[18]. The electrochemical performances are examined in classic carbonate electrolytes, and a constant-voltage discharge (CVDi) is applied after discharging to 5 mV to fully exhibit the capacity. The discharge curves of K (**Figure 2a**) and Na (**Figure 2b**) ion storage have a similar shape, both consisting of a sloping region between 0.1-0.5 V followed by a plateau at a super low potential of below 0.1 V, as shown in the in dQ/dV profiles (insets in **Figure 2a-b**). It delivers a reversible capacity of 306 mAh g^{-1} for Na ion storage with over 65% of it located in the plateau region. In comparison, the K counterpart shows a short low-voltage plateau, resulting in a lower reversible capacity of 273 mAh g^{-1}.

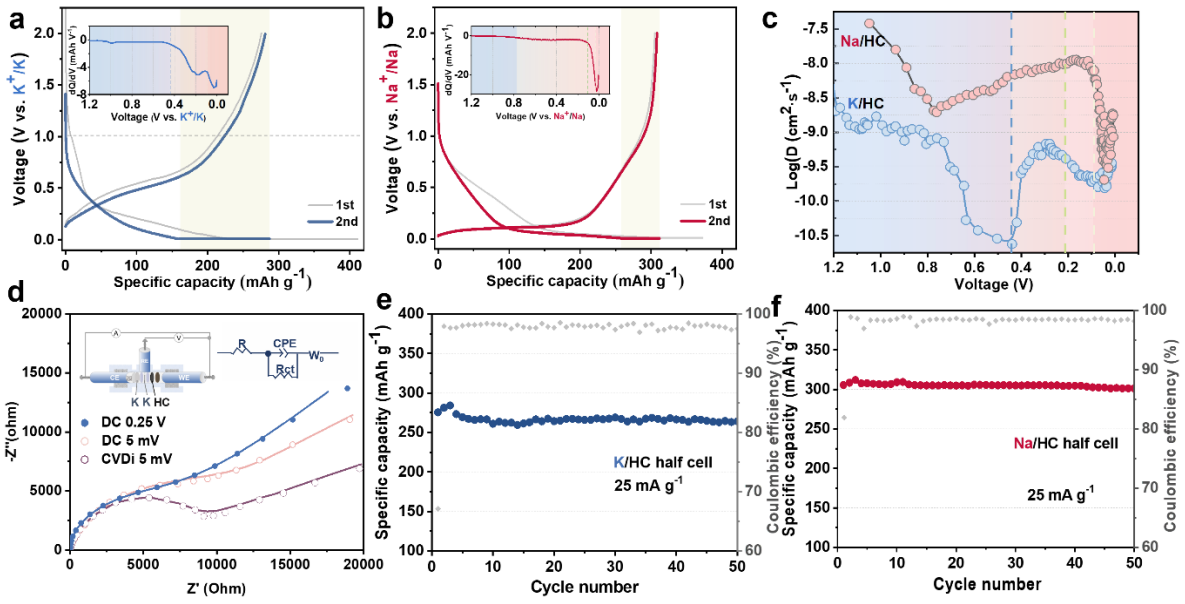

Figure 2. Electrochemical performances and corresponding kinetics. Initial two charging-discharging profiles with insets of dQ/dV profiles for (a) HC-1300/K cell and (b) HC-1300/Na

cell; (c) Diffusion coefficient calculated from GITT results of HC-1300/K cell and HC-1300/Na cell; (d) EIS plots of HC-1300 obtained from the three-electrode cell at different discharging states. Inset illustrates the three-electrode Swagelok cell; Cycling performances of (e) HC-1300/K cell and (f) HC-1300/Na cell.

Apart from the inferior capacity for K ions, a considerable proportion of capacity is gained during the CVDi process because of the poor kinetics. This is also reflected by a large voltage hysteresis between charge/discharge voltage profiles of K-ion cell. Therefore, we measure the apparent diffusion coefficient (D) by a Galvanostatic Intermittent Titration Technique (GITT) technique (**Figure 2c**). Both Na and K ion diffusivities show a similar trend but at a different pace. In specific, upon discharging, both the Na^+ and K^+ diffusivity decreases owing to the formation of SEI[12, 19]. Due to the distinct electrolyte decomposition pathway in the two systems, the Na^+ diffusion pace goes through a progressive reduction above 0.8 V in contrast to 0.4 V for K^+. Afterward, both diffusivity increases at the medium voltage region (0.8-0.1 for Na^+, and 0.45-0.1 V for K^+) because of the fast kinetics associated with Na^+/K^+ adsorption[12]. The insertion-pore filling hybrid mechanism at the low voltage regime leads to a first decrease and then an increase in the diffusivity of both Na^+ and K^+. Overall, the D value for K ion is in general one order of magnitude lower than that for Na, explaining the large voltage hysteresis. We therefore use electrochemical impedance spectroscopy (EIS) to compare the kinetics at the sloping and plateau region. A three-electrode Swagelok cell, consisting of an HC-1300 working electrode, a K metal counter electrode, and a K metal reference electrode, is adopted to avoid the interference of K metal counter electrode (illustrated in the inset of **Figure 2d**). The charge-transfer resistance (R_{ct}) of the sample ramps obviously from 6902 Ohm in the sloping region to over 10000 Ohm once discharging to 5 mV.

Considering such sluggish kinetics in the low-voltage region, the CVDi process is required to fully access the K ion storage capability of HC-1300.

Despite the lower capacity and poor kinetics, the K ion storage possesses similar stability as the Na ion (**Figure 2e-f**), suggesting that the large K ion insertion does not bring about significant structural damage to hard carbon upon cycling. The relatively low efficiencies may lie in the instability of electrolytes[20, 21], which require further optimization. It is worth mentioning that the K ion storage delivers a high charge capacity of 220 mAh g^{-1} below 1.0 V with a relatively high initial Coulombic efficiency of 67.1%, which is one of the best among biomass-derived hard carbon anodes (**Table S1**).

2.3 K-ion storage behaviors

The alike electrochemical behavior between Na and K poses a question of whether they share analogous charge storage mechanisms. Thanks to the intensive studies on Na-ion batteries[22-25], the mechanisms associated with different voltage regimes in the voltage profiles have been clearly demonstrated. Depending on the microstructure of hard carbon, the sloping region may relate to Na ion storage through either adsorption on the isolated graphene layers or insertion between partially ordered graphitic domains[22, 26]. And the low voltage plateau capacity is widely accepted as the contribution of Na ions filling in the nanopores, i.e., the formation of quasi-Na metal clusters[27]. Such a pore-filling behavior is one of the most stunning features of hard carbon, as it can not only uptake Na ion at a low voltage but induce an exceptional capacity of up to 410 mAh g^{-1} [28]. It would be promising if the same mechanism could be applied to K ion storage, which will offer a potential approach to boost the capacity.

Raman tests were conducted on the samples at different states of potassiation/depotassiation (**Figure 3a-b**). Both the intensity D (I_D) and G (I_G) band of carbon decreases once discharged to

0.5 V because of the electrolyte decomposition to form SEI. Nevertheless, we detect neither apparent variation of the I_D/I_G nor shifting of D and G bands position until discharging to 0.25 V. It indicates that K ions storage within this region arises mainly from the surface adsorption on the isolated graphene sheets or defects, consistent with previous reports[29, 30]. Subsequently, an obvious splitting peak at 1613 cm^{-1} of G band emerges when discharged to 5 mV as an indicator of the stiffening of G-mode, which is caused by the disruption of Born-Oppenheimer expansion in the graphene layer and implies the formation of graphite intercalation compounds (GICs) with high stage number (stage II GIC KC_{24})[31, 32]. As the discharging proceeds to the CVDi stage, a significant downshift of G band is discerned and G band displays an asymmetrical Fanoy resonance shape. Such a phenomenon is typically observed in graphitic carbon anodes, like highly graphitized soft carbon(**Figure S6**), because of the existence of deeply intercalated GICs like stage I KC_8[33, 34]. The intercalation of K ions and electron conveyed to graphitic layers causes the red shift for the G band, which can be ascribed to occupied π^* antibonding bands and weakened C-C bonds and the resonant phono scattering process [35, 36].

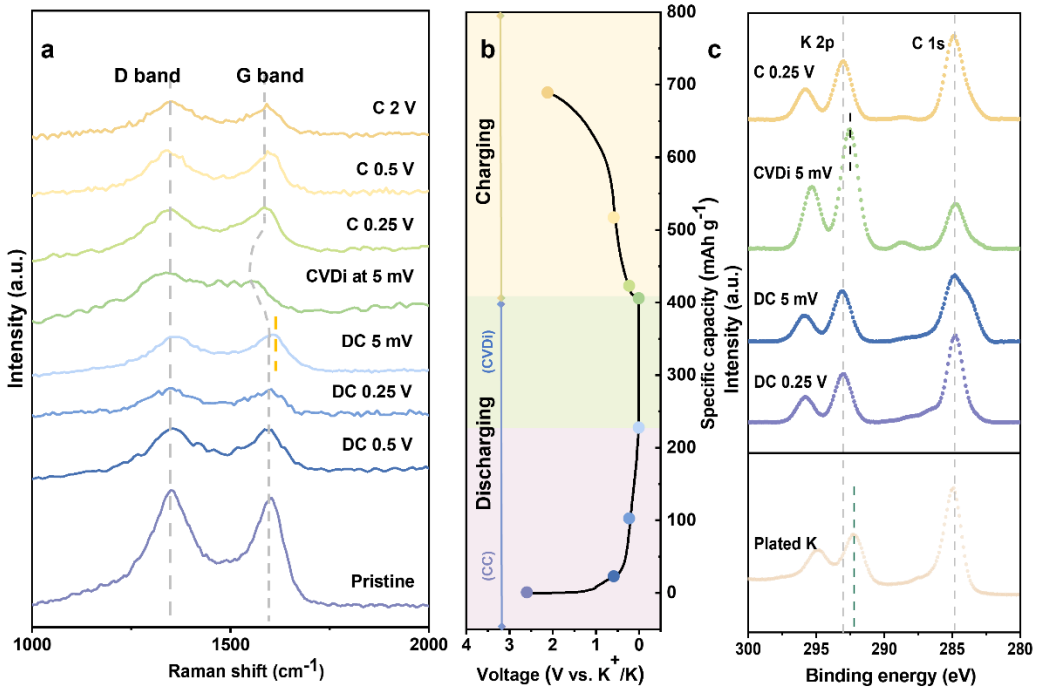

Figure 3. Structural evolution and corresponding K states upon charging/discharging. (a) Ex situ Raman curves of HC-1300/K collected at different charge-discharge states with (b) corresponding charging-discharging profile; (c) Ex situ XPS results of samples at different charge-discharge states after Ar-beam etching with the XPS pattern for plated K as the reference. All the spectra are normalized through C-C peak at 284.8 eV.

To testify whether intercalation could take place in the partially ordered carbon prepared here, we first conducted the ex situ XRD test for the fully discharged sample, the peaks at 30.3° and 33.4° likely ascribed to K-GICs (KC_{24} and KC_8) [37] are detected (**Figure S7**), confirming the intercalation during CVDi process. Then we deliberately plate K metal on HC-1300 electrode by discharging to blow 0 V. A spike is observed in the voltage profile (**Figure S7a**) before the K plating to overcome the nucleation energy, which is widely observed in metal electrode. The absence of such a spike in the cell with CVDi process also excludes the possibility of K metal plating in CVDi process. XRD confirms the plated K metal (**Figure S7b**) after discharging additional merely 30 mAh g^{-1} capacity (based on the weight of HC-1300) below 0 V. The K ion intercalation shows poor kinetics, the reason why a clear shift of G band only appears in the CVDi instead of the constant current discharge stage. When it comes to charging, the G band witnesses a preliminary sudden blue shift at 0.25 V with improved intensity, attributed mainly to the extraction of potassium ions from the graphitic layers. The D and G band positions and their intensity ratio almost recover to the initial stage after charging to 2 V, evidencing the remarkable reversibility. Note that the presence of intercalation cannot exclude pore-filling in the low-voltage region. For instance, the weakening and broadening of the D band in the Raman spectrum after holding at 5 mV could also be associated with the filling of K ions into the nanopores because of the reduced sp^2 ring vibration[22, 38].

XPS was further utilized to detect K states upon charging/discharging. The plated K metal, as discussed before in **Figure S7**, is adopted as a reference to compare with the K ions storage in HC-1300. To avoid the interference of SEI layer, the samples are etched by Ar-beam with a depth of around 40 nm. There is not any clear change of the K 2p peak until discharging to 5 mV. In contrast, we observe the shift of the K 2p peak towards metallic K (**Figure 3c**) of the electrode after CVDi, which cannot be detected without Ar etching (**Figure S8**). The K 2p position is recovered when charging to 0.25 V. This observation indicates the presence of another K form, other than the adsorbed/intercalated K ions and plated K metal, which is most likely to be quasi-metallic K nanoclusters filled in the nanopores according to the similar phenomenon in Na case[39, 40].

We adopted cryo-scanning transmission electron microscopy (cryo-STEM) and electron energy loss spectroscopy (EELS) to probe the detailed charge storage mechanism. The elemental mapping (**Figure 4a**) from energy-dispersive X-ray spectroscopy (EDS) shows the uniform distribution of K element in samples. Compared to the pristine state in **Figure 1b**, the *d*-spacing of {200} plane in the graphitic domain is slightly broadened after discharging to 5 mV, showing a value of 0.39 nm. (**Figure 4b**). This suggests the K-ion intercalation starts before 5 mV, which is confirmed in the corresponding fast Fourier transformation (FFT) pattern: apart from the {200} plane, the {112} plane of KC_{60} (stage V GIC)[41] is observed. The CVDi at 5 mV allows the complete insertion of K ions under slow kinetics, leading to the deep intercalation of K ions into the graphitic domain. The {2117} plane of stage II GIC KC_{24}[41] (inset selected area electron diffraction (SAED) pattern in **Figure 4c**) and {0010} plane of stage I GIC KC_8 (**Figure S9**) are detected after full discharge. It agrees well with the Raman spectra that show a clear G band shift at CVDi, which promotes the sufficient insertion of K ions with sluggish kinetics. The upshift of the C π* peak and the drop of π* intensity after CVDi in the EELS (**Figure 4d-e**) further supports the K ion intercalation. The C

π* peak corresponds to the excitations of electrons from 1*s* to the unoccupied anti-bonding π* of carbon atoms[42]. Its intensity drop indicates the more occupied anti-bonding π* by electrons from alkali ions[43, 44].

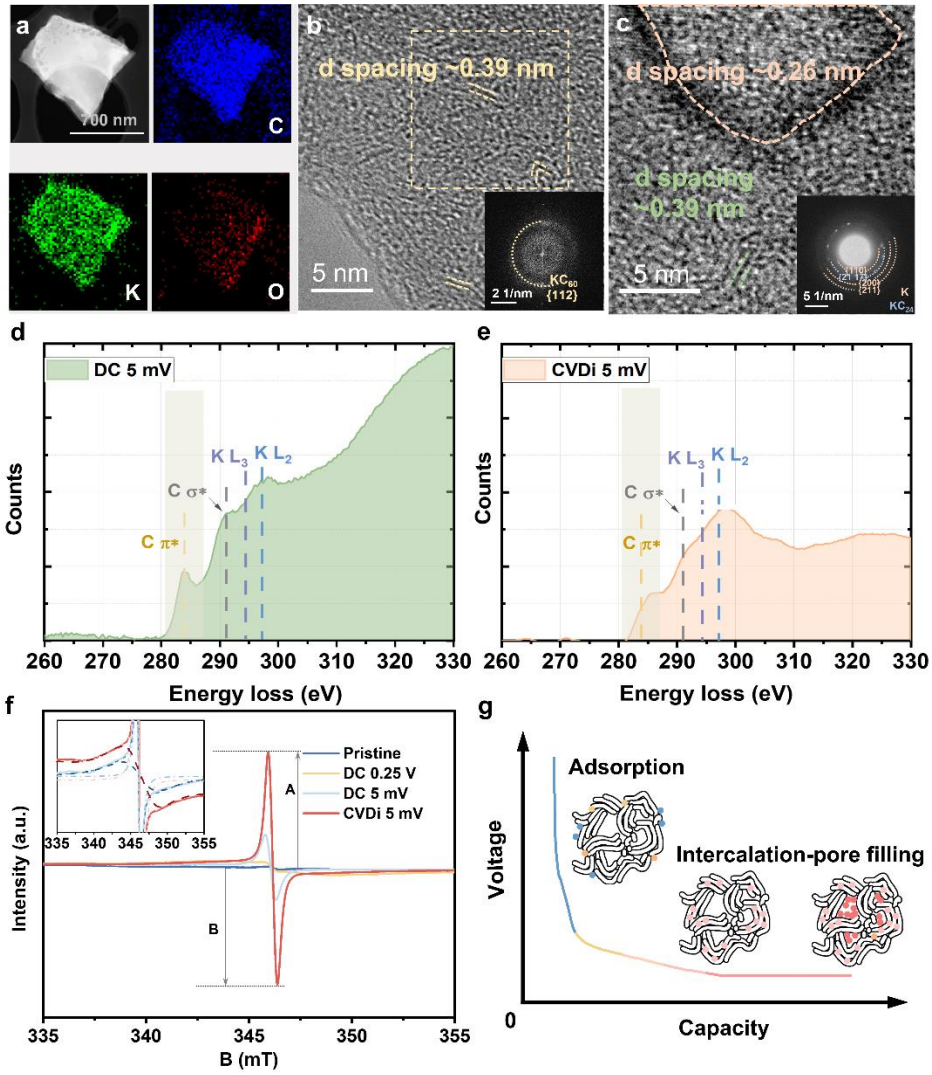

Figure 4. Direct observation of K ion storage behaviors at different voltage regimes. (a) Annular dark-field STEM image and the simultaneous EDS elemental maps for C, K, and O of samples after the CVDi process (CVDi-5 mV); Ex situ HR-TEM images of discharged HC-1300 at 5 mV (b) DC 5 mV sample, with the corresponding FFT pattern (inset), and (c) CVDi 5 mV (K deeper insertion) sample, with the corresponding SAED pattern presented in the inset; EEL spectrum of

(d) DC 5 mV sample and (e) the CVDi 5 mV sample. (All the TEM/STEM observation was taken at cryogenic temperature ~98 K to preserve the pristine state of the samples.) (f) EPR spectra of samples at different cycling states with inset of fitting curves. Each peak (solid line) is deconvoluted into two peaks. The fitted peaks are plotted in dash line with the same color as original data; (g) Schematic illustration of proposed K ion storage behavior along with discharging.

Although detecting the K metal with EELS is challenging because of the lack of reliable potassium reference samples, clear K lattice with diffraction dots have been spotted in high-resolution TEM (HRTEM), which is most likely to be K nanoclusters filled in the nanopores, and is termed as quasi-metallic K following the convention in Na case. Similar quasi-metallic Na nanoclusters in hard carbon were captured by Kang's group before[45]. The lattice spacing of 0.26 nm is well aligned with the {200} plane of the cubic K metal ($Im\bar{3}m$ (229) group) (**Figure 4c**). Furthermore, diffraction patterns corresponding to the {110}, {200}, and {211} planes of K metal are captured in the SAEDs (The insets in **Figure 4c** and **Figure S9b**). To the best of our knowledge, this is the first direct observation of quasi-metallic potassium storage in carbon-based electrodes.

Additionally, the signal of quasi-metallic K after CVDi (**Figure 4f**) is also detected through EPR, a powerful technique to capture the unpaired or delocalized electrons for alkali metal and transition metal elements[46]. The pristine sample exhibits no pronounced signal but a tiny defect one originating from functional groups[47]. As discharge proceeds, the broad peak ($\Delta B_{pp} \approx 5.1$ mT) in Lorentz line shape (The absolute ratio of the maximum to the minimum of the intensity (A/B) is about unity) emerges, which represents more delocalized π-electrons of graphitic crystallites after K intercalation[14]. This broad peak becomes more pronounced after the CVDi process as shown in the inset of **Figure 4f,** which indicates the existence of GICs of low stage number in the

CVDi stage due to the stronger interaction between the σ-spin of K^+ with π-electrons in the graphitic molecule[48], consistent with the above-mentioned Raman and XRD results. Notably, a new sharp narrow peak ($\Delta B_{pp} \approx$ 0.8 mT) centered at a *g*-value of 2.00193 appears after discharge to 5 mV. It becomes strongly intense after CVDi due to the presence of delocalized electrons around the inserted K ions as a result of partial electron transfer from the hard carbon to the inserted K ions (from K^+ to $K^{(1-x)+}$, $0<x<1$, the form of quasi metallic K) in deep discharge[39, 49]. Moreover, the symmetrical Lorentz shape (A=B) is obviously distinguished from the Dysonian asymmetrical shape (A>B) of the large bulk metal[50], which suggests the quasi-metallic K clusters are nanoscale not plated bulk ones[51]. Based on the above discussion, apart from the adsorption in the sloping region, it can be interpreted that "intercalation-pore filling" hybrid behavior occurs in the low-voltage region, and the former starts first (**Figure 4g**).

3. Discussion

Having confirmed the presence of K ion pore filling in HC-1300, we next discuss whether such phenomenon exists in other hard carbon anodes and the approaches to promote the pore filling for gaining a high capacity at the low-voltage region.

i). Universality of K ion pore filling. To examine whether K ion filling in the nanopores occurs in other types of hard carbon, we prepared the lignin-derived one (Lig-HC) following the previous work[52]. Similar to the results on HC-1300 derived from pistachio, an over 50 mAh g^{-1} capacity is delivered in the low-voltage plateau of Lig-HC (**Figure 5a**). A K 2p peak shift is found in XPS after CVDi process, indicating the presence K pore-filling behavior in hard carbon derived from different precursors.

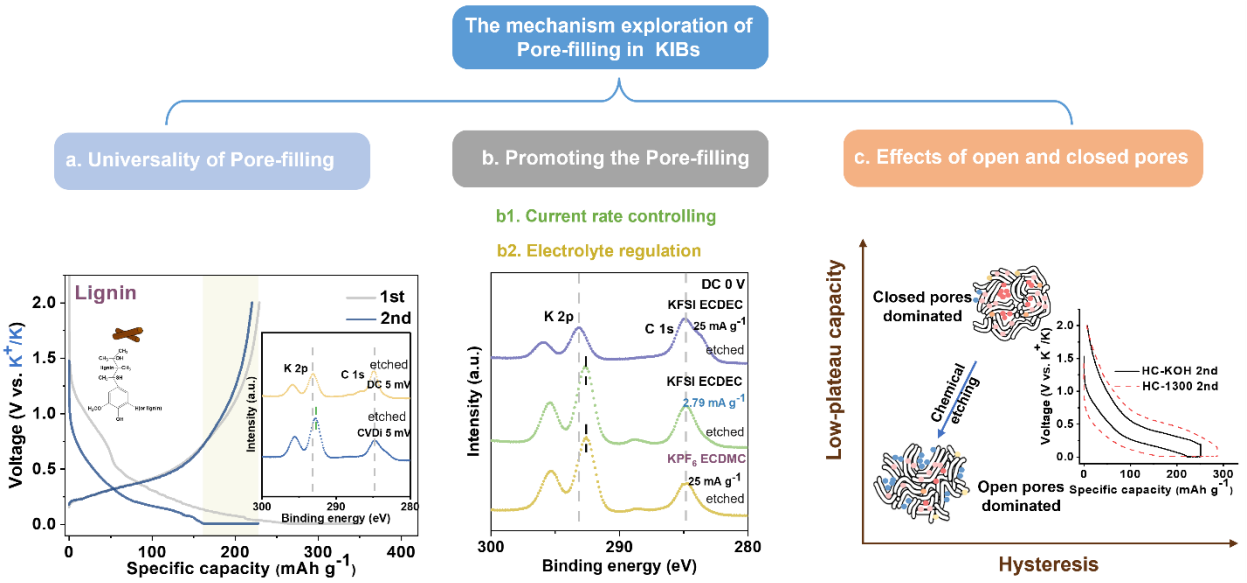

Figure 5. Further exploration of pore-filling mechanism. (a) The validity of pore-filling; (b) Strategies to avoid CVDi; (c) Effects of open and closed pores. To avoid the interference of SEI layer, the samples for XPS tests are etched by Ar-beam with a depth of around 40 nm.

ii). Promoting the pore-filling behavior. The long duration of CVDi might restrict the practical utilization. We investigate whether CVDi is essential for such K storage behavior from two aspects. First, we directly discharge the HC-1300 at an extremely low current of 2.79 mA g^{-1} (~1/100 C) to 0 V (**Figure S10**). An obvious shift of the K 2p peak suggests that the pore filling of K ions could take place without CVDi. Furthermore, the charge transfer kinetics is affected by the SEI, which is closely related to the electrolyte formulation[53]. Our preliminary investigations show that 0.8 M KPF_6 in EC/DMC helps the construction of robust SEI favoring the K ions transfer (**Figure 5b**). It allows the K ion pore filling at a relatively large constant current density of 25 mA g^{-1} (voltage profiles are presented in **Figure S10**). Therefore, the pore filling of K ions could be realized without resorting to the CVDi through further electrolyte engineering to circumvent the slow kinetics.

iii). Effects of open and closed pores. After clarifying the validity of the pore-filling mechanism, a question remains whether we could improve the K ion storage capacity by increasing the porosity. We apply the classic chemical activation by KOH to create additional pores as potential active sites, and the sample is denoted as HC-KOH with an over ten-times improved BET surface area (**Figure S11**). The HC-KOH sample shows a much-reduced voltage hysteresis in the charge/discharge curves (**Figure 5c and Figure S12**). This does not come as a surprise as the high porosity could shorten the solid diffusion path to ameliorate the kinetics, leading to small polarization and high rate capability[54]. Nevertheless, the chemical activation fails to promote the K ion pore-filling, as evidenced by the short low-voltage plateau. We speculate that only closed pores could be utilized for hosting the K ions as the studies on Na ion pore-filling have already demonstrated the overwhelming role of closed pores in determining the low-voltage plateau capacity[18, 55]. Additionally, we calculated the closed pore volume of the HC-KOH from the helium pycnometer-based true density test. It shows an increased true density of 2.16 g cm^{-3}, indicating a decreased closed pore volume of 0.02 cm^3 g^{-1}, which is over 50% reduced compared to the value (0.043 cm^3 g^{-1}) for HC-1300. Such a dramatic decrease in closed pore volume might limit the pore-filling behavior (**Figure 5c**), thus calling for the preparation of hard carbon with rich closed pores to boost the capacity in future studies. Note that the voltage hysteresis of hard carbon is slightly larger than graphite and soft carbons, which should be correlated to a lower electronic conductivity in HC with a poor graphitization degree. Apart from the chemical etching method and electrolyte optimation mentioned before, the higher proportion of conductive materials in the electrode may also reduce the voltage hysteresis. To verify it, we increase the conductive carbon (SP) content from 5% to 30%. A slightly reduced voltage hysteresis is observed (**Figure S13**). The

higher capacity in the 30% SP-containing HC electrode is due to the capacity contribution by carbon SP[56].

4. Conclusion

We prepare a hard carbon material from pistachio shell waste for exploring the K ion storage performance and the associated charge storage mechanism. It is found that the K ion insertion exhibits much lower kinetics than the Na ion, requiring a CVDi at the end of discharge to allow the full K ion insertion. The as-prepared anode delivers a decent charging capacity of over 200 mAh g^{-1} at below 1 V, making biomaterials-derived hard carbons attractive candidates for low-cost KIBs. Furthermore, pore structural tests indicate the presence of rich pores in the sample, providing an ideal plateau form to explore the pore-filling mechanism. Such a mechanism has been widely observed in Na ion storage but is controversial in the K ion counterpart. Assisted by the cryo-TEM and EPR, we clearly observe the quasi-potassium nanoclusters after fully discharging, evidencing that the K ion filling could also occur in the hard carbon. Such behavior could be promoted through optimizing cycling protocol and electrolyte engineering to circumvent poor kinetics. We also show that the open pores created through classic chemical etching do not enhance the pore-filling capacity but only boost the kinetics. It indicates the design of appropriate closed pores is the key to achieving high-capacity hard carbon in future studies.

References

[1] J.M. Tarascon, M. Armand, Issues and Challenges Facing Rechargeable Lithium Batteries, Nature 414(6861) (2001) 359-367. https://doi.org/10.1038/35104644.

[2] L. Deng, T. Wang, Y. Hong, M. Feng, R. Wang, J. Zhang, Q. Zhang, J. Wang, L. Zeng, Y. Zhu, L. Guo, A Nonflammable Electrolyte Enabled High Performance $K_{0.5}MnO_2$ Cathode for

Low-Cost Potassium-Ion Batteries, ACS Energy Letters 5(6) (2020) 1916-1922. https://doi.org/10.1021/acsenergylett.0c00912.

[3] R. Zhou, H. Tan, Y. Gao, Z. Hou, X. Du, B. Zhang, Constructing Resilient Solid Electrolyte Interphases on Carbon Nanofiber Film for Advanced Potassium Metal Anodes, Carbon 186 (2022) 141-149. https://doi.org/10.1016/j.carbon.2021.10.023.

[4] K. Kubota, M. Dahbi, T. Hosaka, S. Kumakura, S. Komaba, Towards K-Ion and Na-Ion Batteries as "Beyond Li-Ion", The Chemical Record 18(4) (2018) 459-479. https://doi.org/10.1002/tcr.201700057.

[5] L. Wang, J. Yang, J. Li, T. Chen, S. Chen, Z. Wu, J. Qiu, B. Wang, P. Gao, X. Niu, H. Li, Graphite as a Potassium Ion Battery Anode in Carbonate-based Electrolyte and Ether-based Electrolyte, Journal of Power Sources 409 (2019) 24-30. https://doi.org/10.1016/j.jpowsour.2018.10.092.

[6] J.L. Yang, Z.C. Ju, Y. Jiang, Z. Xing, B.J. Xi, J.K. Feng, S.L. Xiong, Enhanced Capacity and Rate Capability of Nitrogen/Oxygen Dual-Doped Hard Carbon in Capacitive Potassium-Ion Storage, Advanced Materials 30(4) (2018) 1700104. https://doi.org/10.1002/adma.201700104.

[7] H. Tan, X. Du, R. Zhou, Z. Hou, B. Zhang, Rational Design of Microstructure and Interphase Enables High-capacity and Long-life Carbon Anodes for Potassium Ion Batteries, Carbon 176 (2021) 383-389. https://doi.org/10.1016/j.carbon.2021.02.003.

[8] C. Chen, Z. Wang, B. Zhang, L. Miao, J. Cai, L. Peng, Y. Huang, J. Jiang, Y. Huang, L. Zhang, J. Xie, Nitrogen-rich Hard Carbon as a Highly Durable Anode for High-power Potassium-ion Batteries, Energy Storage Materials 8 (2017) 161-168. https://doi.org/10.1016/j.ensm.2017.05.010.

[9] C. Chi, Z. Liu, X. Lu, Y. Meng, C. Huangfu, Y. Yan, Z. Qiu, B. Qi, G. Wang, H. Pang, T. Wei, Z. Fan, Balance of Sulfur Doping Content and Conductivity of Hard Carbon Anode for High-performance K-ion Storage, Energy Storage Materials 54 (2023) 668-679. https://doi.org/10.1016/j.ensm.2022.11.008.

[10] H. Li, Z. Cheng, Q. Zhang, A. Natan, Y. Yang, D. Cao, H. Zhu, Bacterial-Derived, Compressible, and Hierarchical Porous Carbon for High-Performance Potassium-Ion Batteries, Nano Letters 18(11) (2018) 7407-7413. https://doi.org/10.1021/acs.nanolett.8b03845.

[11] S.J.R. Prabakar, S.C. Han, C. Park, I.A. Bhairuba, M.J. Reece, K.-S. Sohn, M. Pyo, Spontaneous Formation of Interwoven Porous Channels in Hard-Wood-Based Hard-Carbon for High-Performance Anodes in Potassium-Ion Batteries, Journal of The Electrochemical Society 164(9) (2017) A2012. https://doi.org/10.1149/2.1251709jes.

[12] D. Saurel, B. Orayech, B. Xiao, D. Carriazo, X. Li, T. Rojo, From Charge Storage Mechanism to Performance: A Roadmap toward High Specific Energy Sodium-Ion Batteries through Carbon Anode Optimization, Advanced Energy Materials 8(17) (2018). https://doi.org/10.1002/aenm.201703268.

[13] J.M. Stratford, P.K. Allan, O. Pecher, P.A. Chater, C.P. Grey, Mechanistic Insights into Sodium Storage in Hard Carbon Anodes Using Local Structure Probes, Chemical Communications 52(84) (2016) 12430-12433. https://doi.org/10.1039/C6CC06990H.

[14] Q. Li, J. Zhang, L. Zhong, F. Geng, Y. Tao, C. Geng, S. Li, B. Hu, Q.-H. Yang, Unraveling the Key Atomic Interactions in Determining the Varying Li/Na/K Storage Mechanism of Hard Carbon Anodes, Advanced Energy Materials 12(37) (2022) 2201734. https://doi.org/10.1002/aenm.202201734.

[15] L.-F. Zhao, Z. Hu, W.-H. Lai, Y. Tao, J. Peng, Z.-C. Miao, Y.-X. Wang, S.-L. Chou, H.-K. Liu, S.-X. Dou, Hard Carbon Anodes: Fundamental Understanding and Commercial Perspectives for Na-Ion Batteries beyond Li-Ion and K-Ion Counterparts, Advanced Energy Materials 11(1) (2021) 2002704. https://doi.org/10.1002/aenm.202002704.

[16] Nagmani, A. Tyagi, S. Puravankara, Insights into the Diverse Precursor-based Micro-spherical Hard Carbons as Anode Materials for Sodium–ion and Potassium–ion Batteries, Materials Advances 3(2) (2022) 810-836. https://doi.org/10.1039/D1MA00731A.

[17] P. Debye, H.R.A. Jr., H. Brumberger, Scattering by an Inhomogeneous Solid. II. The Correlation Function and Its Application, Journal of Applied Physics 28(6) (1957) 679-683. https://doi.org/10.1063/1.1722830.

[18] M. Yuan, B. Cao, H. Liu, C. Meng, J. Wu, S. Zhang, A. Li, X. Chen, H. Song, Sodium Storage Mechanism of Nongraphitic Carbons: A General Model and the Function of Accessible Closed Pores, Chemistry of Materials 34(7) (2022) 3489-3500. https://doi.org/10.1021/acs.chemmater.2c00405.

[19] L. Fan, R. Ma, Q. Zhang, X. Jia, B. Lu, Graphite Anode for a Potassium-Ion Battery with Unprecedented Performance, Angewandte Chemie International Edition in English 58(31) (2019) 10500-10505. https://doi.org/10.1002/anie.201904258.

[20] Y. Hu, L. Fan, A.M. Rao, W. Yu, C. Zhuoma, Y. Feng, Z. Qin, J. Zhou, B. Lu, Cyclic-anion Salt for High-voltage Stable Potassium-metal Batteries, National Science Review 9(10) (2022) nwac134. https://doi.org/10.1093/nsr/nwac134.

[21] M. Gu, A.M. Rao, J. Zhou, B. Lu, In Situ Formed Uniform and Elastic SEI for High-Performance Batteries, Energy & Environmental Science 16(3) (2023) 1166-1175. https://doi.org/10.1039/D2EE04148K.

[22] X. Chen, J. Tian, P. Li, Y. Fang, Y. Fang, X. Liang, J. Feng, J. Dong, X. Ai, H. Yang, Y. Cao, An Overall Understanding of Sodium Storage Behaviors in Hard Carbons by an "Adsorption-Intercalation/Filling" Hybrid Mechanism, Advanced Energy Materials (2022). https://doi.org/10.1002/aenm.202200886.

[23] S. Alvin, H.S. Cahyadi, J. Hwang, W. Chang, S.K. Kwak, J. Kim, Revealing the Intercalation Mechanisms of Lithium, Sodium, and Potassium in Hard Carbon, Advanced Energy Materials 10(20) (2020) 2000283. https://doi.org/10.1002/aenm.202000283.

[24] Y. Morikawa, S.i. Nishimura, R.i. Hashimoto, M. Ohnuma, A. Yamada, Mechanism of Sodium Storage in Hard Carbon: An X-Ray Scattering Analysis, Advanced Energy Materials 10(3) (2019). https://doi.org/10.1002/aenm.201903176.

[25] J.L. Xia, D. Yan, L.P. Guo, X.L. Dong, W.C. Li, A.H. Lu, Hard Carbon Nanosheets with Uniform Ultramicropores and Accessible Functional Groups Showing High Realistic Capacity and Superior Rate Performance for Sodium-Ion Storage, Advanced Materials 32(21) (2020) e2000447. https://doi.org/10.1002/adma.202000447.

[26] C. Matei Ghimbeu, J. Górka, V. Simone, L. Simonin, S. Martinet, C. Vix-Guterl, Insights on the Na^+ Ion Storage Mechanism in Hard Carbon: Discrimination between the Porosity, Surface Functional Groups and Defects, Nano Energy 44 (2018) 327-335. https://doi.org/10.1016/j.nanoen.2017.12.013.

[27] M. Anji Reddy, M. Helen, A. Groß, M. Fichtner, H. Euchner, Insight into Sodium Insertion and the Storage Mechanism in Hard Carbon, ACS Energy Letters 3(12) (2018) 2851-2857. https://doi.org/10.1021/acsenergylett.8b01761.

[28] Q. Meng, Y. Lu, F. Ding, Q. Zhang, L. Chen, Y.-S. Hu, Tuning the Closed Pore Structure of Hard Carbons with the Highest Na Storage Capacity, ACS Energy Letters 4(11) (2019) 2608-2612. https://doi.org/10.1021/acsenergylett.9b01900.

[29] S. Huang, Z. Li, B. Wang, J. Zhang, Z. Peng, R. Qi, J. Wang, Y. Zhao, N-Doping and Defective Nanographitic Domain Coupled Hard Carbon Nanoshells for High Performance Lithium/Sodium Storage, Advanced Functional Materials 28(10) (2018) 1706294. https://doi.org/10.1002/adfm.201706294.

[30] Z. Yu, Q. Liu, C. Chen, Y. Zhu, B. Zhang, Regulating the Interfacial Chemistry Enables Fast-Kinetics Hard Carbon Snodes for Potassium Ion Batteries, Journal of Power Sources 557 (2023) 232592. https://doi.org/10.1016/j.jpowsour.2022.232592.

[31] Q. Li, Y. Zhang, Z. Chen, J. Zhang, Y. Tao, Q.-H. Yang, Discrete Graphitic Crystallites Promise High-rate Ion Intercalation for KC_8 Formation in Potassium Ion Batteries, Advanced Energy Materials 12(35) (2022) 2201574. https://doi.org/10.1002/aenm.202201574.

[32] J.C. Chacón-Torres, L. Wirtz, T. Pichler, Manifestation of Charged and Strained Graphene Layers in the Raman Response of Graphite Intercalation Compounds, ACS Nano 7(10) (2013) 9249-9259. https://doi.org/10.1021/nn403885k.

[33] H. Tan, R. Zhou, B. Zhang, Understanding Potassium Ion Storage Mechanism in Pitch-derived Soft Carbon and the Consequence on Cyclic Stability, Journal of Power Sources 506 (2021) 230179. https://doi.org/10.1016/j.jpowsour.2021.230179.

[34] K. Share, A.P. Cohn, R.E. Carter, C.L. Pint, Mechanism of Potassium Ion Intercalation Staging in Few Layered Graphene from in Situ Raman Spectroscopy, Nanoscale 8(36) (2016) 16435-16439. https://doi.org/10.1039/C6NR04084E.

[35] S. Komaba, W. Murata, T. Ishikawa, N. Yabuuchi, T. Ozeki, T. Nakayama, A. Ogata, K. Gotoh, K. Fujiwara, Electrochemical Na Insertion and Solid Electrolyte Interphase for Hard-Carbon Electrodes and Application to Na-Ion Batteries, Advanced Functional Materials 21(20) (2011) 3859-3867. https://doi.org/10.1002/adfm.201100854.

[36] L.J. Hardwick, P.W. Ruch, M. Hahn, W. Scheifele, R. Kotz, P. Novak, In Situ Raman Spectroscopy of Insertion Electrodes for Lithium-ion Batteries and Supercapacitors: First Cycle Effects, Journal of Physics and Chemistry of Solids 69(5-6) (2008) 1232-1237. https://doi.org/10.1016/j.jpcs.2007.10.017.

[37] H. Onuma, K. Kubota, S. Muratsubaki, W. Ota, M. Shishkin, H. Sato, K. Yamashita, S. Yasuno, S. Komaba, Phase Evolution of Electrochemically Potassium Intercalated Graphite, Journal of Materials Chemistry A 9(18) (2021) 11187-11200. https://doi.org/10.1039/D0TA12607A.

[38] Z. Xu, J. Wang, Z. Guo, F. Xie, H. Liu, H. Yadegari, M. Tebyetekerwa, M.P. Ryan, Y.S. Hu, M.M. Titirici, The Role of Hydrothermal Carbonization in Sustainable Sodium‐Ion Battery Anodes, Advanced Energy Materials 12(18) (2022) 2200208. https://doi.org/10.1002/aenm.202200208.

[39] Z. Wang, X. Feng, Y. Bai, H. Yang, R. Dong, X. Wang, H. Xu, Q. Wang, H. Li, H. Gao, C. Wu, Probing the Energy Storage Mechanism of Quasi-Metallic Na in Hard Carbon for Sodium-Ion Batteries, Advanced Energy Materials 11(11) (2021) 2003854. https://doi.org/10.1002/aenm.202003854.

[40] Q. Li, X. Liu, Y. Tao, J. Huang, J. Zhang, C. Yang, Y. Zhang, S. Zhang, Y. Jia, Q. Lin, Y. Xiang, J. Cheng, W. Lv, F. Kang, Y. Yang, Q.-H. Yang, Sieving Carbons Promise Practical

Anodes with Extensible Low-potential Plateaus for Sodium Batteries, National Science Review 9(8) (2022) nwac084. https://doi.org/10.1093/nsr/nwac084.

[41] J. Liu, T. Yin, B. Tian, B. Zhang, C. Qian, Z. Wang, L. Zhang, P. Liang, Z. Chen, J. Yan, X. Fan, J. Lin, X. Chen, Y. Huang, K.P. Loh, Z.X. Shen, Unraveling the Potassium Storage Mechanism in Graphite Foam, Advanced Energy Materials 9(22) (2019) 1900579. https://doi.org/10.1002/aenm.201900579.

[42] Z. Feng, Y. Lin, C. Tian, H. Hu, D. Su, Combined Study of the Ground and Excited States in the Transformation of Nanodiamonds into Carbon Onions by Electron Energy-loss Spectroscopy, Scientific Reports 9(1) (2019) 3784. https://doi.org/10.1038/s41598-019-40529-2.

[43] T. Nonaka, H. Kawaura, Y. Makimura, Y.F. Nishimura, K. Dohmae, In Situ X-ray Raman Scattering Spectroscopy of a Graphite Electrode for Lithium-ion Batteries, Journal of Power Sources 419 (2019) 203-207. https://doi.org/10.1016/j.jpowsour.2019.02.064.

[44] A. Hightower, C.C. Ahn, B. Fultz, P. Rez, Electron Energy-loss Spectrometry on Lithiated Graphite, Applied Physics Letters 77(2) (2000) 238-240. https://doi.org/10.1063/1.126936.

[45] Y.S. Yun, K.-Y. Park, B. Lee, S.Y. Cho, Y.-U. Park, S.J. Hong, B.H. Kim, H. Gwon, H. Kim, S. Lee, Y.W. Park, H.-J. Jin, K. Kang, Sodium-Ion Storage in Pyroprotein-Based Carbon Nanoplates, Advanced Materials 27(43) (2015) 6914-6921. https://doi.org/10.1002/adma.201502303.

[46] G. Feher, A.F. Kip, Electron Spin Resonance Absorption in Metals. I. Experimental, Physical Review 98(2) (1955) 337-348. https://doi.org/10.1103/PhysRev.98.337.

[47] K. Kawamura, Electron Spin Resonance Behavior of Pitch-based Carbons in the Heat Treatment Temperature Range of 1100–2000 °C, Carbon 36(7) (1998) 1227-1230. https://doi.org/10.1016/S0008-6223(98)00103-1.

[48] Y.-P. Wu, C.-R. Wan, C.-Y. Jiang, S.-B. Fang, Y.-Y. Jiang, Mechanism of Lithium Storage in Low Temperature Carbon, Carbon 37(12) (1999) 1901-1908. https://doi.org/10.1016/S0008-6223(99)00067-6.

[49] E. Zhecheva, R. Stoyanova, J.M. Jiménez-Mateos, R. Alcántara, P. Lavela, J.L. Tirado, EPR Study on Petroleum Cokes Annealed at Different Temperatures and Used in Lithium and Sodium Batteries, Carbon 40(13) (2002) 2301-2306. https://doi.org/10.1016/S0008-6223(02)00121-5.

[50] Z.-E. Yu, Y. Lyu, Y. Wang, S. Xu, H. Cheng, X. Mu, J. Chu, R. Chen, Y. Liu, B. Guo, Hard Carbon Micro-nano Tubes Derived from Kapok Fiber as Anode Materials for Sodium-ion Batteries and the Sodium-ion Storage Mechanism, Chemical Communications 56(5) (2020) 778-781. https://doi.org/10.1039/C9CC08221B.

[51] A. Niemöller, P. Jakes, R.-A. Eichel, J. Granwehr, EPR Imaging of Metallic Lithium and its Application to Dendrite Localisation in Battery Separators, Scientific Reports 8(1) (2018) 14331. https://doi.org/10.1038/s41598-018-32112-y.

[52] X. Lin, Y. Liu, H. Tan, B. Zhang, Advanced Lignin-derived Hard Carbon for Na-ion Batteries and a Comparison with Li and K Ion Storage, Carbon 157 (2020) 316-323. https://doi.org/10.1016/j.carbon.2019.10.045.

[53] L. Fan, H. Xie, Y. Hu, Z. Caixiang, A.M. Rao, J. Zhou, B. Lu, A Tailored Electrolyte for Safe and Durable Potassium Ion Batteries, Energy & Environmental Science 16(1) (2023) 305-315. https://doi.org/10.1039/D2EE03294E.

[54] A. Hatanaka, Y. Elakneswaran, K. Kurumisawa, T. Nawa, The Impact of Tortuosity on Chloride Ion Diffusion in Slag-Blended Cementitious Materials, Journal of Advanced Concrete Technology 15(8) (2017) 426-439. https://doi.org/10.3151/jact.15.426.

[55] Y. Li, Y. Lu, Q. Meng, A.C.S. Jensen, Q. Zhang, Q. Zhang, Y. Tong, Y. Qi, L. Gu, M.M. Titirici, Y.S. Hu, Regulating Pore Structure of Hierarchical Porous Waste Cork-Derived Hard Carbon Anode for Enhanced Na Storage Performance, Advanced Energy Materials 9(48) (2019). https://doi.org/10.1002/aenm.201902852.

[56] Y. Xu, C. Zhang, M. Zhou, Q. Fu, C. Zhao, M. Wu, Y. Lei, Highly Nitrogen Doped Carbon Nanofibers with Superior Rate Capability and Cyclability for Potassium Ion Batteries, Nature Communications 9(1) (2018) 1720. https://doi.org/10.1038/s41467-018-04190-z.